Geophysical Journal International

Geophys. J. Int. (2010) **180,** 1187–1199 doi: 10.1111/j.1365-246X.2009.04468.x

Assessment of tomographic mantle models using spectral element seismograms

Ebru Bozdağ* and Jeannot Trampert

Department of Earth Sciences, Utrecht University, PO Box 80021, NL-3508 *TA, Utrecht, the Netherlands. E-mail: bozdag@princeton.edu*

Accepted 2009 December 1. Received 2009 August 31; in original form 2008 October 9

SUMMARY

We investigated the agreement between real seismograms and those predicted by long wavelength mantle models by looking at phase and amplitude differences. We computed full synthetic seismograms using a spectral element method together with 3-D mantle models and the appropriate crustal model on top. We selected differently damped mantle models to see the effect of regularization on the computed seismograms. To check the phase agreement, we measured time-shifts between the real and synthetic surface waves and body wave phases such as *P, S* and *SS* using a cross-correlation technique. We also compared the amplitudes of the real and synthetic seismograms to understand how well the models explain not only the phases, but the whole waveforms. 3-D mantle models improve the phase agreement of surface waves in particular. The remaining misfit, however, is still so large that we cannot distinguish between different tomographic models. We suggest that this is mainly due to an imperfect modelling of the crust, and/or source location if body waves are included, which have to be addressed in future inversions. Amplitude mismatches are large, regardless which 3-D mantle model is used. We observe that 3-D scattering or focusing/defocusing effects can only explain half of the surface wave amplitudes whereas body wave amplitudes are dominated by scattering effects. 1-D Q models, particularly in the crust and upper-mantle, strongly affect surface wave amplitudes and have to be modelled properly.

Key words: Body waves; Surface waves and free oscillations; Seismic tomography; Computational seismology; Wave propagation; Crustal structure.

1 INTRODUCTION

The global mantle structure has extensively been studied by seismic tomography. With an increasing number of high-quality data in recent years, the resolution of the images has considerably improved. Nevertheless, in practice, the resolution of the models is still largely determined by the details of the inverse algorithm. Without exception, all current global models are based upon some approximation to the wave equation. Due to its simplicity and ease of implementation, ray theory has been used in most tomographic studies which has provided robust images of long wavelength structure of the Earth's mantle (see recent reviews by Romanowicz 2003; Trampert & van der Hilst 2005). Including finite frequency effects is the next desirable step (e.g. Montelli *et al.* 2004; Zhou *et al.* 2005; Sigloch *et al.* 2008), but at long wavelengths, models remain largely independent of the implemented approximation in the forward problem. Due to the uneven data coverage, models are far more dependent on the regularization of the inverse problem (Trampert & Spetzler 2006). Different models are also parametrized in various ways, but their good correlation, at least at long wavelengths (e.g. Ritzwoller & Lavely 1995; Becker & Boschi 2002), suggests that the chosen mathematical description of the model has the least influence. Although damping plays a critical role in the final models, it is done in a somewhat arbitrary way. The aim of our study is to establish if we can identify an optimally damped model based on comparisons between predicted and real seismograms.

Current computer facilities and recent advances in numerical methods allow us to simulate wave propagation in complex 3-D earth models without any approximations to the wave equation. Ideally, this new tool should directly be used for imaging. Although efforts started to be made on a local and regional scale (e.g. Tape *et al.* 2007; Fichtner *et al.* 2008), the computational cost remains high for global studies. A first step towards using these new techniques is to establish how well current models are predicting observed seismograms and what the remaining signal is. A few isolated comparisons between real and synthetic seismograms have been shown (e.g. Komatitsch & Tromp 2002b; Komatitsch *et al.* 2002, 2005; Tsuboi *et al.* 2003, 2004), and the first quantitative comparison of 3-D mantle models has been published by Qin *et al.* (2009) who looked at long period minor and major arc surface wave predictions ($T > 100$ s). They compared 3-D long wavelength mantle models from different groups in terms of the average phase and amplitude anomalies for a few selected earthquakes.

*Now at: Department of Geosciences, Princeton University, Guyot Hall, Princeton, NJ 08544, USA.

We present a quantitative assessment of 3-D models based on comparisons between real and synthetic seismograms to see if we can identify an optimal regularization and establish how large the unexplained signal is. This will hopefully lead to a strategy towards a full waveform inversion. The computation of the synthetic seismograms was performed with the spectral element code (SEM) by Komatitsch & Tromp (2002a,b). We selected four differently damped mantle models (Trampert & Spetzler 2006) which we superimposed on top of transversely isotropic PREM (Dziewonski & Anderson 1981). We also computed synthetic seismograms using the independent 3-D mantle model S20RTS (Ritsema *et al.* 1999), which unofficially is often considered a reference 3-D model. During the simulations, all mantle models were used together with the 3-D crustal model Crust2.0 (Bassin *et al.* 2000). In addition, we computed synthetic seismograms using PREM alone and PREM together with Crust2.0 to isolate the effect of the 3-D models. Our analysis is performed in the period range of 40–200 s in accordance with the spectral content of the data used in the construction of the models. Rather than looking at the overall fit to the complete seismograms, we separated surface and body (*P, S SS*) waves and examined their phase and amplitude misfits.

In the following section, we briefly describe the tomographic models used in this study. In Section 3, we illustrate how the phase and amplitude measurements were carried out and in Section 4, we present our results based on the measured time-shifts and the amplitude misfits. Finally, we discuss our results before presenting some general conclusions.

2 MODELS ENTERING THE CALCULATION OF THE SYNTHETIC SEISMOGRAMS

We calculated SEM seismograms using four mantle models obtained for different levels of horizontal damping [see brown curve in Fig. 1 in Trampert & Spetzler (2006)]. The models were constructed from about 1.5 million Rayleigh wave phase velocity measurements of fundamental modes (Trampert & Woodhouse 1995) and the first five overtones (van Heijst & Woodhouse 1999). 2-D finite frequency kernels (Spetzler *et al.* 2002) were used for phase velocity and asymptotic kernels for depth. In cross-sections of the four mantle models (Fig. 1), it is clearly seen that highly damped models are smoother, whereas smaller damping causes the amplitude of the models to increase and introduces more small-scale heterogeneities. Model m_1 is built from 780 independent parameters and would correspond to one selected by a cautious seismologist who prefers smooth models. Model m_2 has a trace of the resolution of 1752 and would correspond to a model chosen by a criterion of maximum curvature of the L-curve. Model m_3 is built from 3108 independent parameters corresponds to a point where the reduced χ^2 does not significantly change any more. Finally, model m_4 is

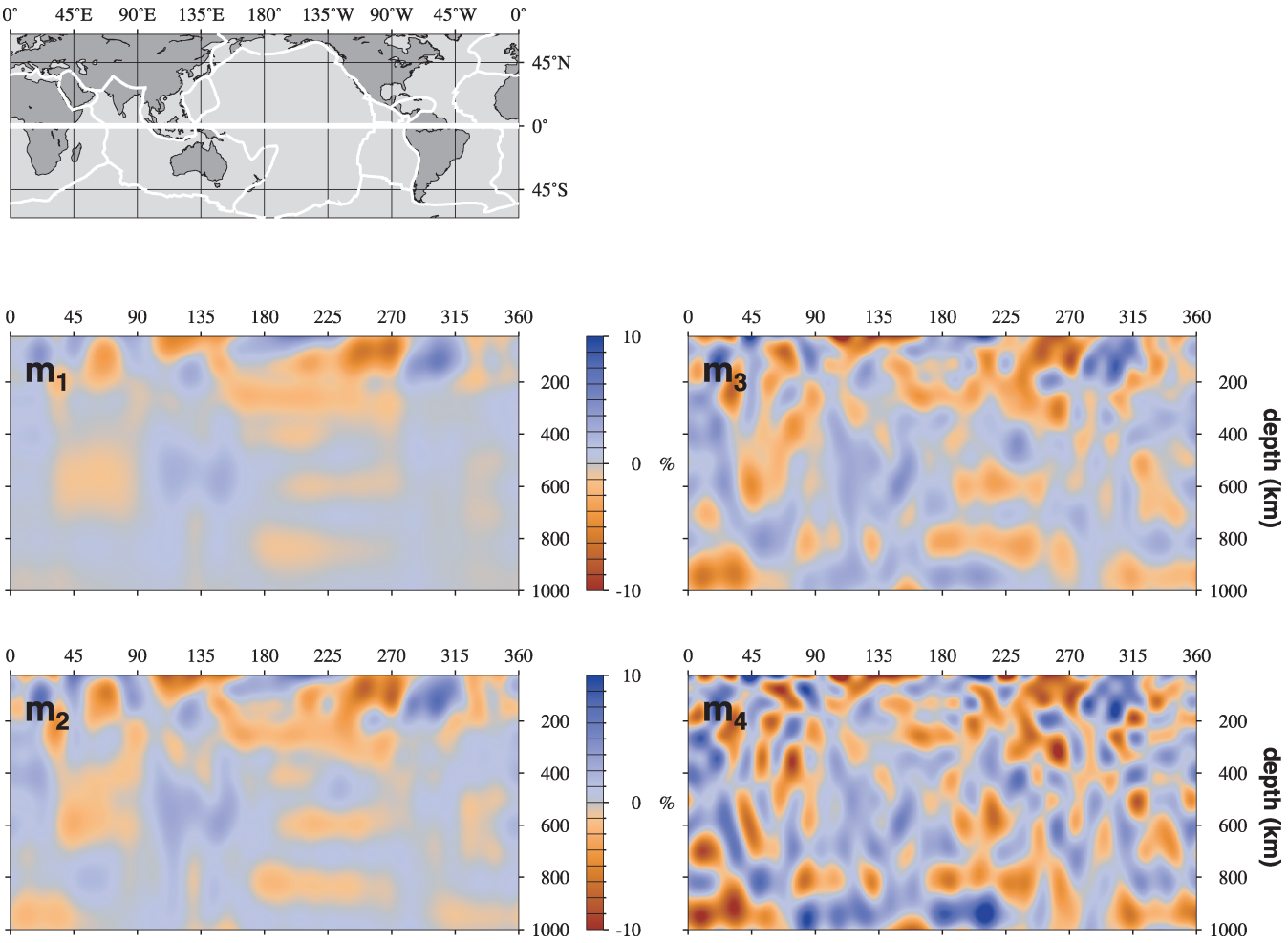

Figure 1. Sample cross-sections of the selected mantle models of Trampert & Spetzler (2006) along the equator. From m_1 to m_4, damping decreases.

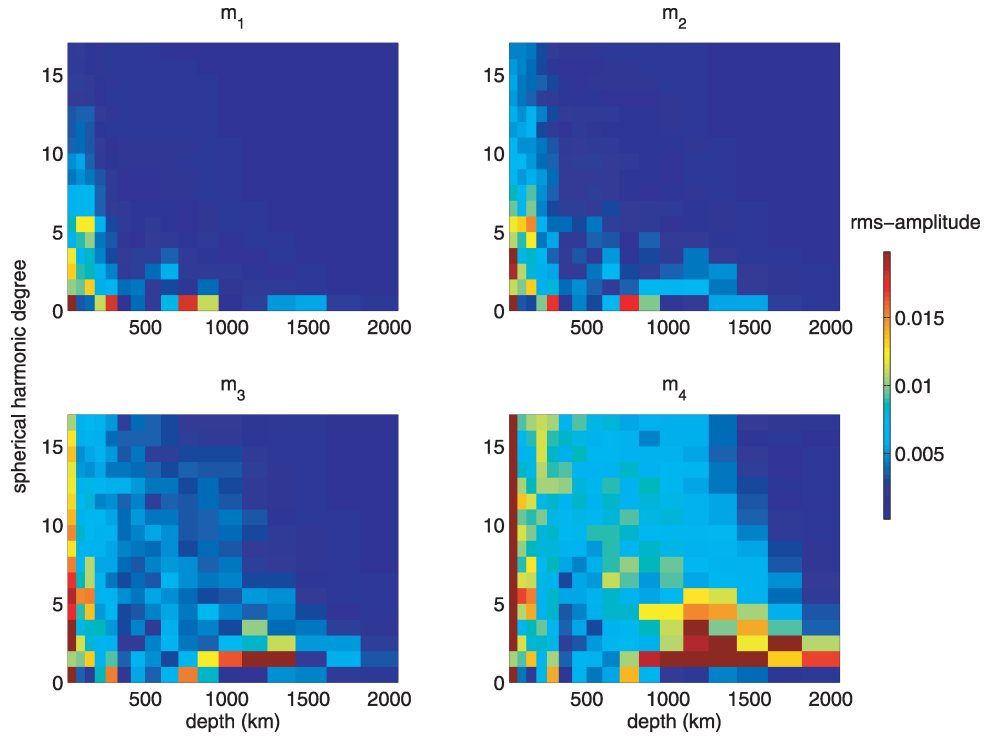

Figure 2. Rms-amplitudes of the mantle models of Trampert & Spetzler (2006) as a function of depth and spherical harmonic degree. From m_1 to m_4, damping decreases.

constructed from 4489 independent parameters and is so rough that everybody would agree that instabilities are occurring. These models would obviously lead to different geological interpretations. The properties of the models and differences between them are best seen on the amplitude spectra plotted for different depths and spherical harmonic degrees (Fig. 2). From smooth to rough, the amplitude of the models gradually increases. The upper part of the models shows large differences. Below 1000 km depth, the sensitivity of the data to mantle structure diminishes and this is where instabilities start to develop. This is particularly evident for model m_4 with significant amplitude for low spherical harmonic degrees in the mid-mantle. The synthetic seismograms corresponding to these four mantle models for a sample source–receiver path are shown in Fig. 3 where changes both in phase and amplitude are observed for body and surface waves. Crustal corrections were applied to the phase velocity data prior to inversion by calculating the exact eigen

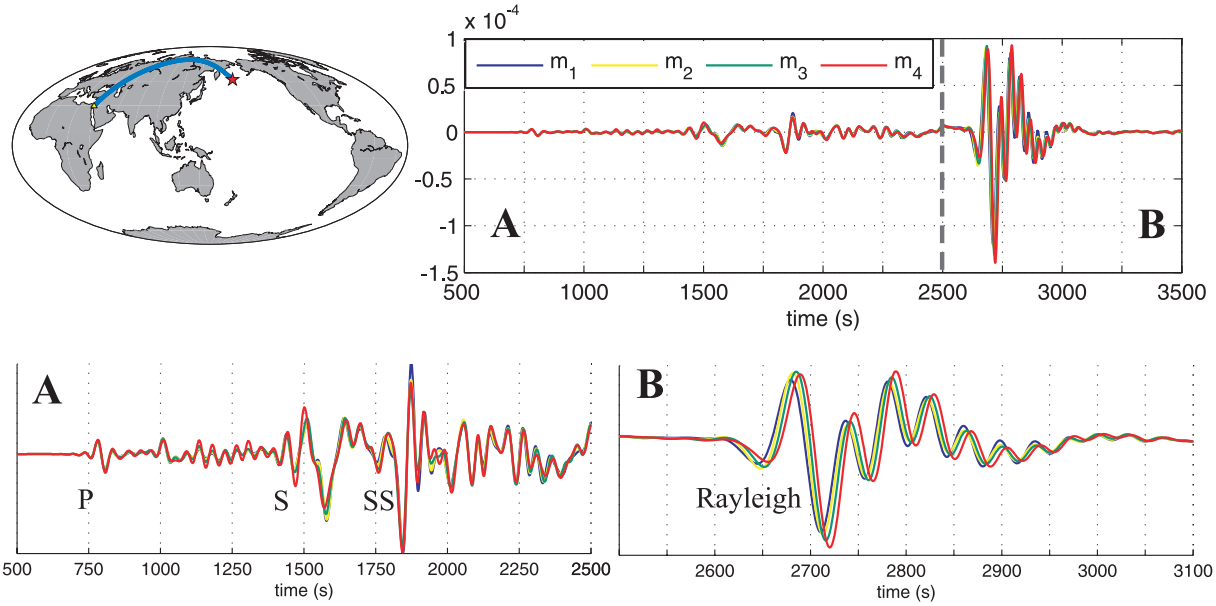

Figure 3. SEM seismograms computed for the selected mantle models of Trampert & Spetzler (2006) for the Rat Islands earthquake (2003 March 17, $M_w = 7.0$) recorded at the station EIL ($\Delta = 93^\circ$). Body waves and Rayleigh waves are enlarged in A and B, respectively to show the effect of damping more clearly on the computed seismograms.

Table 1. List of earthquakes selected from the global CMT catalogue (www.globalcmt.org).

Event name	Region	Date	Moment magnitude (M_w)	Depth (km)
111600B	New Ireland Region	16/11/2000	8.0	24
120600C	Turkmen SSR	06/12/2000	7.0	33
010901G	Vanuatu Islands	09/01/2001	7.0	114
011101A	Vancouver Island Region	11/01/2001	6.0	24
021801B	Prince Edward Islands Region	18/02/2001	6.0	15
022401A*	Molucca Passage	24/02/2001	7.0	43
101201E	South of Mariane Islands	12/10/2001	7.0	42
110901A	Panama – Costa Rica Border	09/11/2001	6.0	17
091602E	Near N Coast of Papua New Guinea	16/09/2002	6.0	15
012703A	Turkey	27/01/2003	6.0	15
031703E*	Rat Islands, Aleutian Islands	17/03/2003	7.0	27
042403B	Kuril Islands	24/04/2003	6.0	44
062003D	Western Brazil	20/06/2003	7.0	556
103103A	Off East Coast of Honshu	31/10/2003	7.0	15
020504B*	Irian Jaya Region, Indonesia	05/02/2004	7.0	13
030804D	Northern Mid-Atlantic Ridge	08/03/2004	6.0	12
032704G	Xizang	27/03/2004	6.0	12
042704D	Vanuatu Islands	27/04/2004	6.0	17
100904E*	Near Coast of Nicaragua	09/10/2004	6.9	39
110904F	Solomon Islands	09/11/2004	6.9	12
112804I*	Hokkaido, Japan Region	28/11/2004	7.0	47
200602222219A*	Mozambique	22/02/2006	7.0	12
200608200341A	Scotia Sea	20/08/2006	7.0	17
200612261226A	Taiwan Region	26/12/2006	6.9	20

Notes: Corresponding broad-band vertical component seismograms were obtained through IRIS (www.iris.edu) and synthetic seismograms were computed using the spectral element code by Komatitsch & Tromp (2002a,b). Synthetic seismograms for PREM, PREM+Crust2.0 and S20RTS models were only computed for earthquakes marked by a star (*).

frequencies at each grid point of Crust5.1 (Mooney *et al.* 1998) and integrating the crustal phase along the great circle path. In the computation of the full SEM seismograms, we added the 3-D crustal model Crust2.0 (Bassin *et al.* 2000) on top of the 3-D mantle models. Crust5.1 and Crust2.0 are very similar except for differences in grid resolution and sediments. This will not affect our results since the period range we considered is not sensitive enough to perceive the difference. We also computed synthetic seismograms with an independent mantle model S20RTS (Ritsema *et al.* 1999) which is parametrized in the same way as the models of Trampert & Spetzler (2006) and has the same crustal correction. S20RTS, in addition, includes body wave and normal mode data and used a different smoothing strategy (norm damping). To appreciate the prediction power of 1-D and 3-D crustal models alone, we also computed synthetic seismograms using PREM alone and PREM with Crust2.0 (hereafter called PREM+Crust2.0) on top. In all calculations, we included gravity, attenuation, oceans, topography and bathymetry, ellipticity and rotation (except in PREM alone, we did not use topography and bathymetry) to obtain seismograms as realistic as possible. The length of the synthetic seismograms is 60 min and the sampling rate is 0.26 s. Based on the mesh we used, the shortest period in our synthetics is approximately 30 s.

3 MEASURING MISFITS

3.1 Comparing real and SEM seismograms

We checked the agreement between real and synthetic seismograms by examining phase and amplitude differences. We compared 1374 pairs of seismograms using 22 shallow (CMT depth $\leq$50 km) and two deep (CMT depth $>$50 km) earthquakes having moment magnitudes between 6 and 8 (Table 1) for the selected 3-D mantle models from Trampert & Spetzler (2006). The distribution of earthquakes and stations used to compute the synthetic seismograms is presented in Fig. 4. For S20RTS, PREM+Crust2.0 and PREM models, we only computed synthetic seismograms for a restricted number of earthquakes (see Table 1). To avoid interferences with multiple-orbit waves, caustic, source and receiver effects, we only considered source–receiver pairs with distances between $20^\circ < \Delta < 160^\circ$. For body waves, we used less source–receiver pairs because *P, S* and *SS* phases cannot be observed on all seismograms at all distances. We further restricted epicentral distances to have turning points above 2000 km, the maximum depth where our models change.

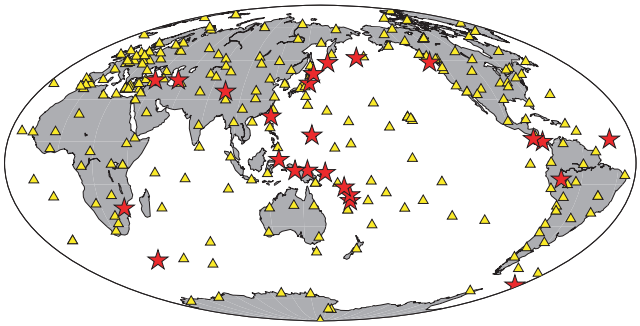

Figure 4. Distribution of earthquakes (stars) and stations (triangles) used to compute synthetic seismograms.

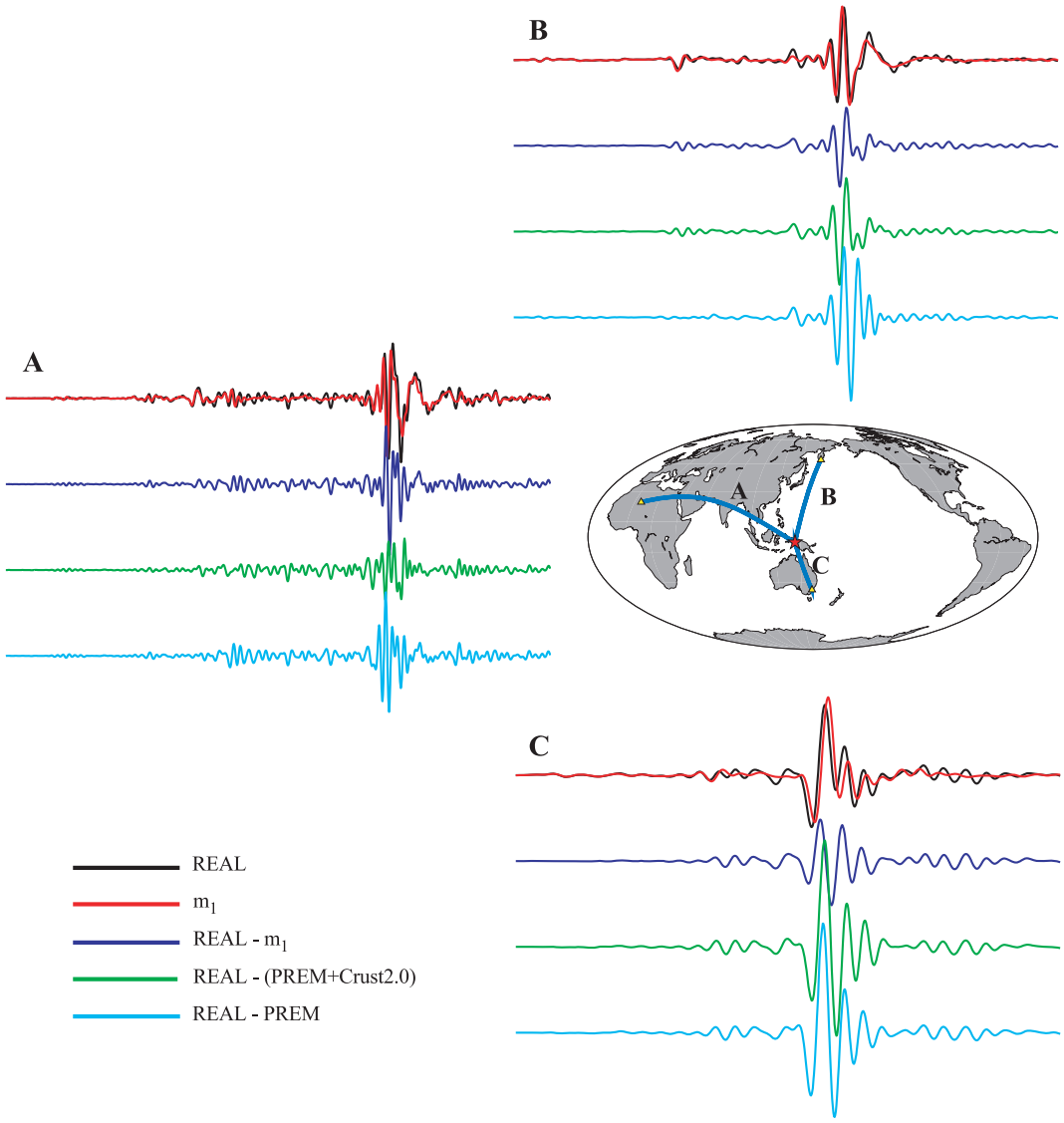

Figure 5. Waveform differences between real and SEM seismograms computed for the mantle model m_1 of Trampert & Spetzler (2006) with Crust2.0 (Bassin *et al.* 2000) on top (blue), PREM (Dziewonski & Anderson 1981) with Crust2.0 on top (green), and PREM alone (cyan). The top traces are real (black) and SEM seismograms computed for m_1 (red). The earthquake (star) (Irian Jaya Region, 2004 February 5, $M_w = 7.0$) and the ray paths to the stations (triangles) (a) TAM ($\Delta = 128^\circ$), (b) PET ($\Delta = 60^\circ$) and CcCAN ($\Delta = 34^\circ$) are shown in the map.

We used broad-band vertical-component seismograms (sampling rate = 0.05 s) as real data. Data having high noise level or glitches were removed manually by comparing them to the synthetic seismograms. The Global CMT solution parameters were used to generate the SEM seismograms. To make the real and SEM seismograms comparable, we followed five steps: (1) We deconvolved the instrument response from the real seismograms. (2) We convolved the SEM seismograms with a Gaussian source time function with the half duration of each earthquake taken from the Global CMT solution. (3) We downsampled the real and the SEM seismograms, whose original sampling rates are 0.05 and 0.26 s, respectively, to a common sampling rate of 1.3 s. (4) We applied a bandpass filter to both real and SEM seismograms between 35 and 300 s to analyse the data in the period range 40–200 s. (5) After synchronizing the real and SEM seismograms, we applied a common time window to make sure that the files contain the same number of points. In Fig. 5, sample synthetic seismograms from 1-D and 3-D models are compared to the real ones in terms of waveform difference. As can clearly be seen, not only surface waves but also body waves are in good agreement both in phase and amplitude for the case of the 3-D mantle model m_1 although it is constructed by surface wave phase velocity measurements only. However, the waveform comparisons between the real and synthetic seismograms reveal clear mismatches. The mismatch from m_1 is, in general, smaller than those from PREM and PREM+Crust2.0 however there still remains a large unexplained part in the seismograms. Instead of looking at the waveform differences of the complete seismograms, which tend to be dominated by the high amplitude part of the signal such as surface waves, we preferred to separate the phase and amplitude information to quantify the agreement between the seismograms. Therefore, in our assessments, we considered fundamental mode Rayleigh waves and body wave phases *P, S* and *SS* separately.

3.2 Measuring time-shifts

We examined the phase difference of surface and body waves in different ways. For surface waves, we first applied a time-variable filter (Cara 1973) to both the real and SEM seismograms to extract the fundamental mode Rayleigh waves. We then took the Fourier transform of the surface waves which can be presented in terms of an amplitude (A) and a phase (ϕ)

$$S_{\rm real}(\omega) = A_{\rm real}(\omega)\exp[{\rm i}\phi_{\rm real}(\omega)] \tag{1}$$

and

$$S_{\rm SEM}(\omega) = A_{\rm SEM}(\omega)\exp[{\rm i}\phi_{\rm SEM}(\omega)], \tag{2}$$

where subscripts 'real' and 'SEM' represent the real and synthetic seismograms, respectively and ω is the angular frequency. To determine the phase shift between these two seismograms, we cross-correlated $S_{\rm real}(\omega)$ with $S_{\rm SEM}(\omega)$ and measured the phase of the cross-correlogram as a function of frequency. After unwrapping the phase, the time-shifts between real and SEM seismograms are obtained by dividing the phase of the cross-correlogram by the angular frequency

$$\delta t_{\rm Rayleigh}(\omega) = \frac{\phi_{\rm real}(\omega) - \phi_{\rm SEM}(\omega)}{\omega}. \tag{3}$$

Because body waves are not as dispersive as surface waves, we measured the time-shift between real and SEM body phases in time domain. We first applied time windows to extract the *P, S* and *SS* phases. The time window was defined sufficiently large around the theoretical arrival times from IASPEI91 (Kennett & Engdahl 1991) to capture the complete pulse. We Fourier transformed both seismograms and applied a Gaussian filter with a central period 60 s. The band-width of the Gaussian filter is 100 per cent of the central period, which means that we consider the full waveform rather than a signal at a specific frequency. We then took the cross-correlation in the frequency domain and after taking the inverse Fourier transform, we measured the time-shift by picking the maximum of the cross-correlogram. We repeated the same procedure for each body wave phase *P, S* and *SS*.

3.3 Measuring amplitude differences

The examination of the amplitude differences between real and synthetic data helps to understand how much the 3-D mantle models contribute to amplitudes. We extracted Rayleigh waves and *P, S* and *SS* as described for the phase shift measurements. After taking the Fourier transform, we calculated the amplitude spectra of the real and SEM seismograms without applying a Gaussian filter. It is more convenient to make the comparisons in the frequency domain since, in a time-series, it is difficult to measure the amplitude independently from the phase which may distort the amplitude measurements. For the amplitude comparisons, we used the expression

$$\chi(\omega) = \ln\left[\frac{A_{\rm real}(\omega)}{A_{\rm SEM}(\omega)}\right] \tag{4}$$

which shows the logarithmic ratio between the real and SEM amplitudes as a function of frequency. For body waves, we only show ratios at 60 s.

4 RESULTS

4.1 Time-shift analysis

For Rayleigh waves, the measured time-shifts corresponding to the four selected models m_1–m_4 are shown as histograms at sample periods 150, 80 and 40 s in Fig. 6. We observe that the phase of the SEM seismograms, in general, match the real ones quite well at long periods. At 150 s, most of the time-shifts are within ±12 s which go

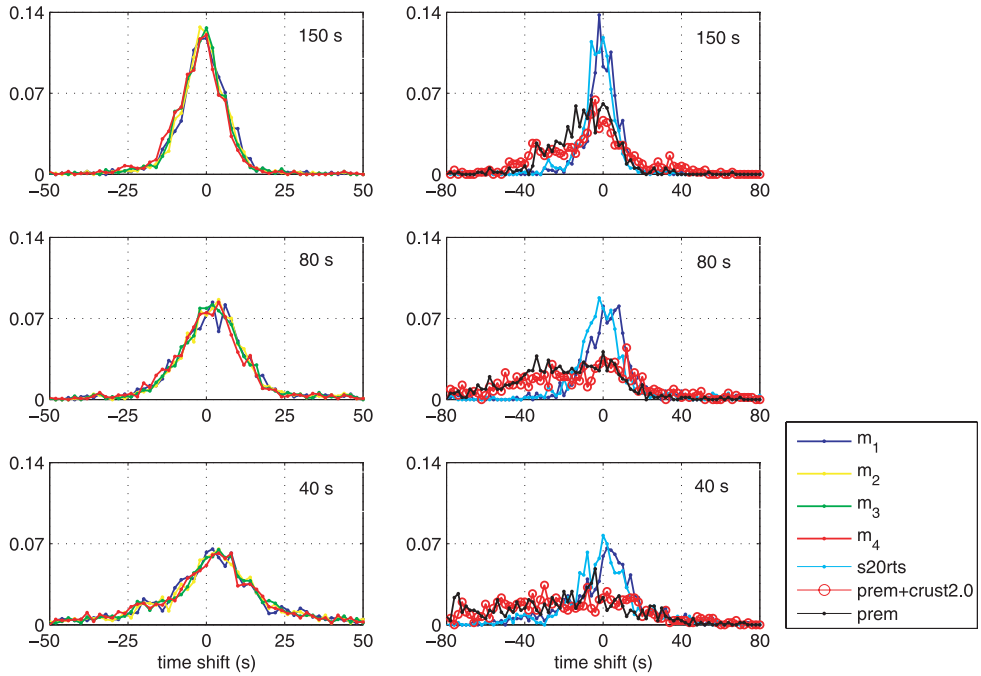

Figure 6. Histograms of Rayleigh wave time-shifts as a function of period measured between real and SEM seismograms computed for the 3-D mantle models m_1 to m_4 (left-hand column) and for various 1-D and 3-D models (right-hand column). Histograms in the right-hand column correspond to the marked earthquakes only in Table 1. From m_1 to m_4, damping decreases. The vertical axis shows the normalized number of measurements so that the histograms integrate to 1.

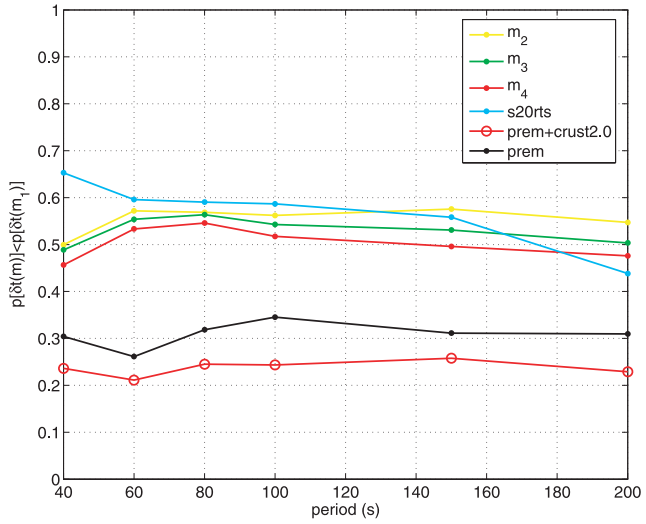

Figure 7. Probabilities that Rayleigh wave time-shifts as a function of period between real and SEM seismograms are smaller than those between real and SEM seismograms computed for the smoothest mantle model m_1.

down to 10 s at 200 s. The discrepancy between the real and SEM seismograms increases with decreasing period and the histograms broaden at 40 s to around ±25 s. Most interestingly, the histograms hardly allow to differentiate between the models. To further appreciate the effect of the 3-D mantle on synthetic seismograms, we computed synthetics in PREM alone, in PREM+Crust2.0 and in S20RTS (obtained from an extended data set and a different regularization strategy) and compared them to the real seismograms in a similar way (Fig. 6). The time-shifts between the real and PREM seismograms can be up to 100 s at short period Rayleigh waves. The histograms also suggest that, on average, there is not much difference between PREM alone and PREM+Crust2.0. It is well known that the crust has a large effect on Rayleigh waves (e.g. Montagner & Jobert 1988; Bozdağ & Trampert 2008), but statistically one is not better off to explain the real data with just a crustal model. It is very clear that a 3-D mantle model is needed to explain the phase of Rayleigh waves. The results from S20RTS are, in general, in agreement with the results from the mantle models of Trampert & Spetzler (2006), particularly at long periods. Slight differences emerge for periods shorter than 100 s. To quantify the difference between the model predictions, we computed the probability that the measured time-shifts between the real and SEM seismograms are smaller than those for the smoothest model m_1. A probability less than 50 per cent means that m_1 is better than the other model. The numbers demonstrate that it is hard to distinguish which mantle model explains the real data best (Fig. 7). Amongst the models of Trampert & Spetzler (2006) a marginally better fit to the real data is obtained by the mantle model m_2. S20RTS shows a slight improvement, particularly at 40 s, but does worse at the longest periods. While the predictions of all 3-D mantle models are very close to each other, synthetics for PREM and PREM+Crust2.0 are much worse, only having a 25 per cent chance of making a better Rayleigh wave prediction than any of the mantle models. It is important to stress that although the model predictions for 3-D mantle models are statistically similar, the model predictions for individual paths are different.

Body waves carry information from deeper parts whereas fundamental mode surface waves are mainly influenced by the first a few hundred km of the mantle. The measured time-shifts between the real and synthetic *P, S* and *SS*-phases are shown as histograms in Fig. 8. *P* waves are, in general, less affected by lateral heterogeneities than *S* waves because the corresponding velocity anomalies are much smaller. The *P*-wave histograms are narrow and vary between ±5 s while those for *SS* waves reach more than ±10 s. In addition, we see a slight shift in the histograms towards positive times similar to surface wave results. S20RTS results are similar to those from m_1. For *P* waves, all model predictions are similar, 1-D or 3-D, and they are surprisingly similar to the corrected measurements which go into the construction of the models (Ritsema, personal communication, 2009). It thus appears that no *P*-wave information is explained by any of the models. This is not surprising, for the models of Trampert & Spetzler (2006) which use a scaling law, but the implementation of S20RTS in SEM uses the model P12 which contains *P*-wave information. The 3-D models clearly explain more of the *S* wave than the *SS*-wave data, but a big parts remain to be modelled. As for surface waves, it is statistically difficult to distinguish which mantle model predicts body wave phases best, but the *S* and *SS* predictions favour the smoother model m_1 and S20RTS over rough models as seen on the scatter plots (Fig. 9).

4.2 Amplitude analysis

We also looked at the amplitude ratios between the real and SEM seismograms for various models. As for the phase measurements, we considered Rayleigh waves, *P, S* and *SS*-phases. In all synthetics, the attenuation model is that of PREM. For Rayleigh waves, all mantle models from Trampert & Spetzler (2006) give similar amplitude misfits (Fig. 10). For long periods, the agreement with the real seismograms is much better (mostly within a factor of 1.5) and as the period decreases the misfits can be up to a factor of 8 at 40 s. In general, the histograms are skewed towards negative values indicating that the Rayleigh wave amplitudes are larger for the SEM seismograms. S20RTS also gives similar results whereas we start to see some slight differences for PREM alone and PREM+Crust2.0 at short periods. A detailed statistical analysis does not show much improvement in amplitude misfits for 3-D models compared to PREM. On average, all models, 1-D or 3-D, give similar probabilities of fit. The slight differences are best seen on scatter plots (Fig. 11). For predicting amplitudes, S20RTS is again more similar to smoother models, as for the phase. The PREM and PREM+Crust2.0 comparisons with m_1 show the most scattering, particularly at 40 s, indicating that there are some differences, but because the scatter plots are symmetric, the probabilities of fit are very close. The difference between the 3-D mantle models can be up to a factor of 1.5 independent of period which is small compared to the observed amplitude anomaly between the real and synthetic seismograms. In the right-hand column of Fig. 10, we present the ratio of PREM/m_1 amplitudes which gives an idea of the scattering or focusing/defocussing effects due to the 3-D crustal and mantle structure together. The total scattering is up to a factor of 2.7, still small compared to the observed amplitude anomalies between the real and synthetic seismograms.

For body waves, we present the amplitude spectra of *P, S* and *SS* waves at 60 s. Mantle models, 1-D or 3-D, again only differ marginally (Fig. 12). Differences are again most pronounced in the scatter plots (Fig. 13). The results from S20RTS are, in general, in agreement with m_1 and the results from PREM and PREM+Crust2.0 only do slightly worse. Statistically 3-D models are not significantly better than 1-D models in estimating the amplitudes of the body waves. Most of the amplitude anomaly for body waves, particularly for *S* and *SS* waves, can be explained by

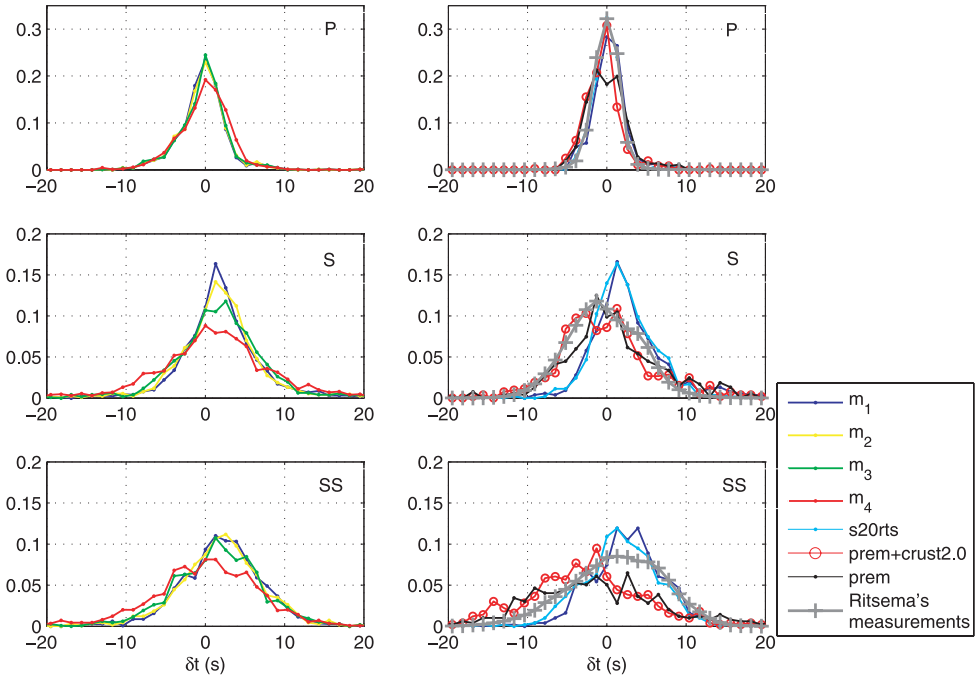

Figure 8. Same as Fig. 6 but for 60 s body waves.

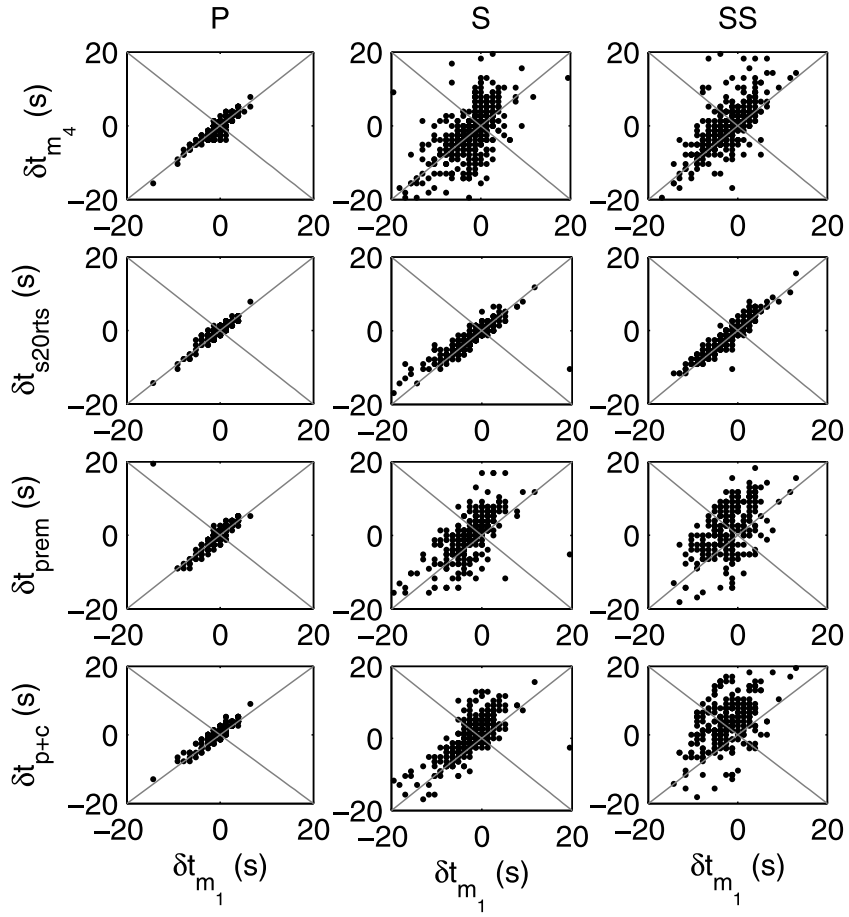

Figure 9. Scatter plots of 60 s body wave time-shifts measured between real and SEM seismograms computed for several 1-D and 3-D models.

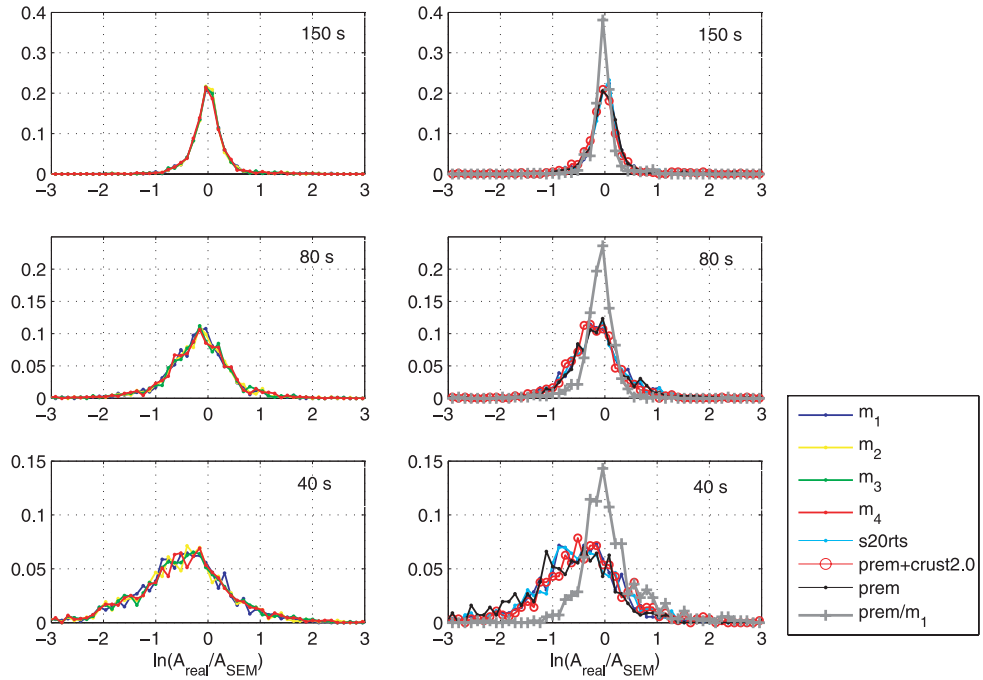

Figure 10. Histograms of Rayleigh wave amplitude ratios as a function of period between real and SEM seismograms computed for the 3-D mantle models m_1 to m_4 (left-hand column) and for various 1-D and 3-D models (right-hand column). Histograms in the right-hand column correspond to the marked earthquakes only in Table 1. From m_1 to m_4, damping decreases. The vertical axis shows the normalized number of measurements so that the histograms integrate to 1.

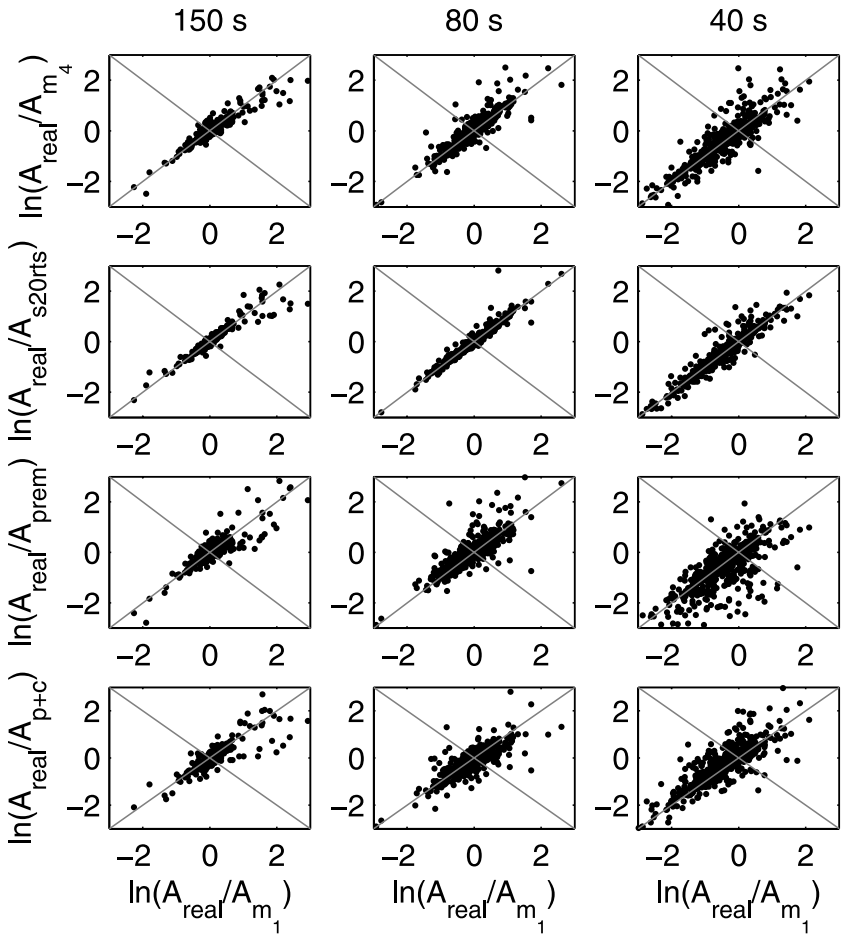

Figure 11. Scatter plots of Rayleigh wave amplitude ratios measured between real and SEM seismograms computed for several 1-D and 3-D models.

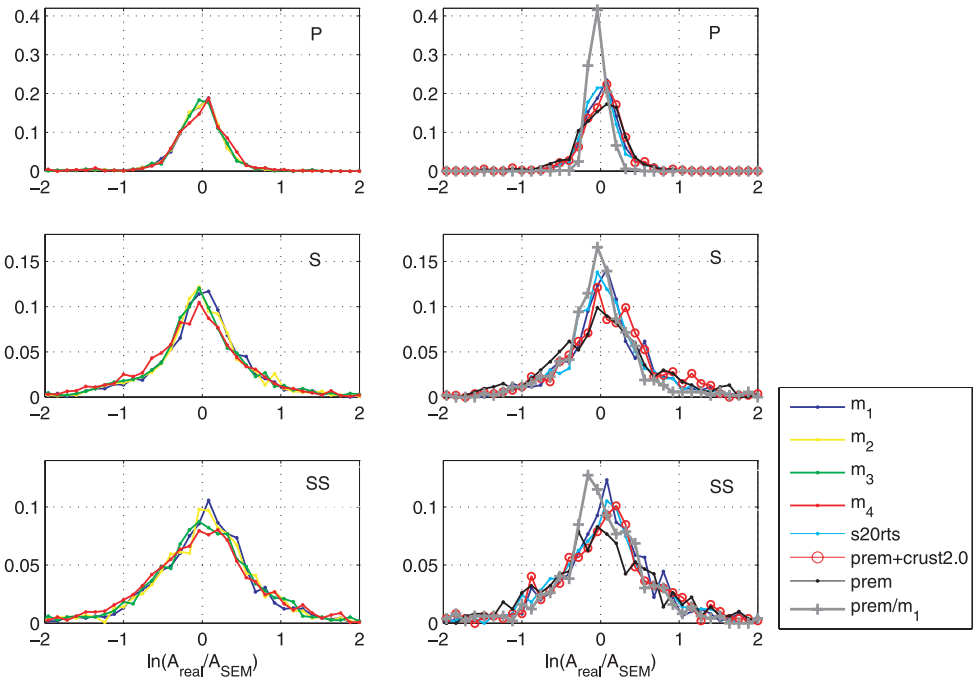

Figure 12. Same as Fig. 10 but for 60 s body waves.

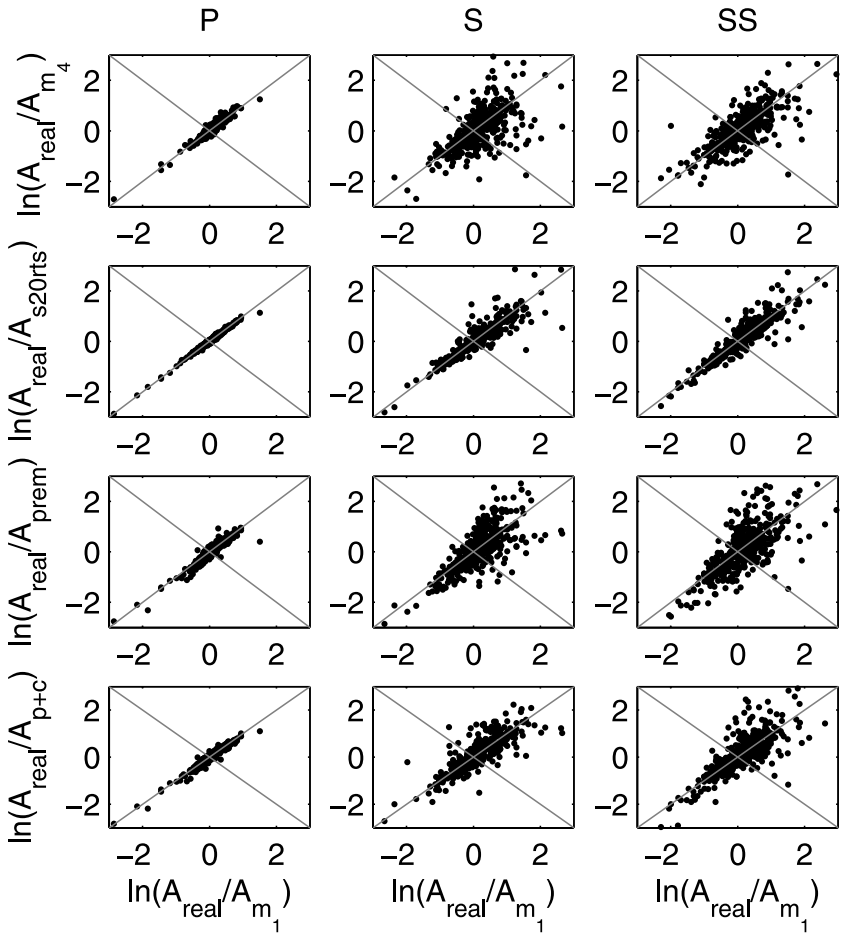

Figure 13. Same as Fig. 11 but for 60 s body waves.

scattering effects as can be seen from the histograms of the ratio of PREM/m_1 amplitudes (Fig. 12).

5 DISCUSSION

It is encouraging to see that the 3-D mantle models bring the synthetic seismograms closer to the observed data in phase, particularly so for surface waves. It is surprising, however, that quite diverse mantle models cannot be distinguished on average (see other model comparisons in Qin *et al.* 2009), although their individual predictions are all different. For amplitudes, 3-D models hardly make any improvements form a statistical point of view, although the scattering or focusing/defocussing effects they produce are not negligible. The question is then what can be done to improve models so that they predict phases and amplitudes much better. Let us first discuss the individual contributions to the phase before turning to the amplitude.

For surface waves, a strong contribution to the overall phase is from the crust in the period range we considered. We observed that the 3-D crust alone does not improve the phase mismatches and a 3-D mantle model is clearly needed. Classical surface wave tomography applies crustal corrections to dispersion measurements before inverting for the mantle structure. Bozdağ & Trampert (2008) showed that these corrections are not perfect and significant errors can map into 3-D mantle structure. While it is clear that the 3-D mantle models improve the phase, compared to PREM+Crust2.0 (Fig. 6), the histograms of unexplained time-shifts are very similar to those incurred by imperfect ray theoretical crustal corrections (Bozdağ & Trampert 2008), both as a function of period and epicentral distance. We believe that the bias due to crustal corrections is the reason why we cannot distinguish between 3-D mantle models. For body waves, although 3-D mantle models improve the phase mismatch between real and synthetic seismograms somewhat, large parts of the signal remain unexplained. A recent paper by Ritsema *et al.* (2009) has shown that finite frequency traveltime delays due to the crust can differ by several seconds from ray theoretical estimations which are used to make crustal corrections in all current models. This suggests that crustal corrections for body waves also need to be revaluated. This discussion assumes that Crust2.0 represents the real Earth which might not be the case of course. Another issue is how the crust is implemented in the SEM code. Capdeville & Marigo (2008) reported that in spectral element methods, different smoothing strategies applied to crustal models may change the response significantly. All in all, it is very likely that the crust is responsible for not being able to distinguish the models, whether it is the crustal correction, the crustal model itself or its implementation in the code. If this is indeed the case, progress to better mantle models can only be made if the crust and mantle are jointly imaged without a correction step.

While the source and receiver phase shifts are correctly modelled in SEM given the source parameters and the velocity model, the surface wave phase measurements which are used to construct the models usually neglect them (e.g. Trampert & Woodhouse 1995; Ekström *et al.* 1997; van Heijst & Woodhouse 1999; Visser *et al.* 2008). A recent study by Ferreira & Woodhouse (2007) has shown that the receiver phase-shift is negligible for both Rayleigh and Love waves. The source phase shift due to lateral heterogeneities around source can be up to 10 s for Rayleigh waves for some specific ray paths as shown by Ferreira & Woodhouse (2006) however, on average, it is small compared to our observed discrepancies. The important question is if we used the right source parameters in SEM. The results of Ferreira & Woodhouse (2007) show that source parameters obtained for more detailed source inversions are compatible with CMT parameters, and therefore do not change the data misfit dramatically. For body waves, it is common to relocate earthquakes during the tomographic inversion or apply relocation corrections as is done for S20RTS. These corrections are of the same order (up to 10 s) as the phase misfits for *P, S* and *SS* waves (Ritsema, personal communication, 2009). While for surface waves the crust is the most likely problem, for body waves these source relocation corrections need to be examined in greater detail.

The amplitude of seismograms depends on elastic and anelastic terms together with source and receiver factors (e.g. Dalton & Ekström 2006). The elastic term, describing the scattering or focusing/defocusing of seismic waves, is due to the lateral heterogeneities in the velocity models (e.g. Woodhouse & Wong 1986; Wang & Dahlen 1995). 3-D attenuation of the Earth's mantle has been investigated using either surface waves (e.g. Romanowicz 1995; Selby & Woodhouse 2000; Gung & Romanowicz 2004; Dalton & Ekström 2006; Dalton *et al.* 2008) or body waves (e.g. Bhattacharyya *et al.* 1996; Reid *et al.* 2001; Warren & Shearer 2002) quantifying the anelastic contribution to amplitudes.

Our results show that, in general, 3-D models do not improve the amplitudes much compared to PREM. Similar observations were reported by Ferreira & Woodhouse (2007), who compared real seismograms with synthetics computed by the great circle approximation and full ray theory, and by Qin *et al.* (2009) based on a spectral element method. For Rayleigh waves, amplitude anomalies due to scattering in the 3-D model are within a factor of 2.7 (Fig. 10). The amplitude differences between real and SEM seismograms are much larger and thus the remaining difference should be due to attenuation, source and receiver effects. Ferreira & Woodhouse (2007) showed that source and elastic contributions are equally important for surface wave amplitudes, but the receiver effects can be neglected for vertical component seismograms. Zhou (2009) computed 3-D sensitivity kernels for phase delays and amplitudes due to anelastic perturbations for fundamental mode surface waves and reported that scattering effects due to 3-D velocity models are larger than those for 3-D anelastic models. The 3-D models have a much larger effect on body wave amplitudes. Especially *S* and *SS* phases are very much affected by scattering. Amplitude anomalies from 3-D models are almost as large as the observed amplitude anomalies between the real and SEM seismograms which confirms the previous studies (e.g. Ritsema *et al.* 2002; Tibuleac *et al.* 2003). We also observed that scattering effects increase with decreasing period. If this is the case, then most of observed amplitude misfit should be due to the uncertainty in source parameters and unexplained elastic structure in the velocity models.

Although amplitudes appear to be less sensitive to 3-D variations in anelastic structure, we wondered about the influence of the 1-D attenuation model. As shown by Resovsky *et al.* (2005), anelasticity in the crust and upper-mantle is poorly constrained in 1-D shear Q models and depending on the data set, Q values can vary between 120 to more than 1000. The crust and upper-mantle could have lower Q than that of PREM (e.g. Durek & Ekström 1996; Resovsky *et al.* 2005). To test if part of the surface wave histograms may be due to the 1-D PREM attenuation, we computed synthetic seismograms by changing the PREM Q model in the first two layers consisting crust and upper-mantle structure from 600 to 200 and 80 to 70, respectively. In Fig. 14, we show the resulting amplitude ratios. The shift in the histograms as a function of period is similar to what we observe for Rayleigh wave amplitudes in Fig. 10. This may also effect 3-D attenuation models which are constructed as a perturbation

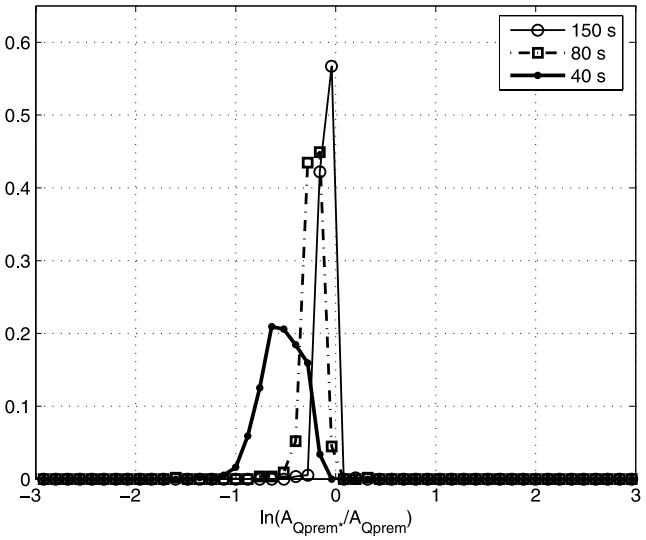

Figure 14. Histograms of Rayleigh wave amplitude ratios as a function of period measured between SEM seismograms computed using the actual (Q_{prem}) and the modified ($Q_{\mathrm{prem}}*$) PREM Q model. In the modified PREM Q model, the crustal and the upper-mantle Q values are set to 200 and 70 whereas in the actual model they are 600 and 80, respectively.

from them. At least 1-D Q models need to be incorporated in all attempts to model surface wave amplitudes.

We do not think that the model parametrization plays a major role in the observed mismatches. Boschi & Dziewonski (1999) reported that most discrepancies due to different parametrizations tend to disappear by a sufficiently strong regularization and discrepancies are most likely to be due to the insufficient data coverage. Qin *et al.* (2009) reported similar misfits for various 3-D models from different groups obtained by different parametrizations, indicating indeed that the latter is of minor consequence.

6 CONCLUSIONS

We made quantitative comparisons between real seismograms and those predicted by various 3-D mantle models using the SEM code. We observed that in particular for surface waves, the models improved the phase mismatch, but surprisingly we could hardly distinguish between the different mantle models. Amplitude discrepancies were little affected by any of the models and even PREM alone made predictions just as good.

Although there is a tendency that smooth models are slightly better, our findings are a good reminder that current tomographic images contain (or lack) a lot of structure because of a certain choice of regularization. While the latter has a dramatic effect on the interpretation, little of the details are currently constraint by the seismograms.

We suggest that imperfect crustal corrections are the most likely reason why we cannot distinguish the models in terms of surface wave phase misfits. For body waves the source location correction may play a big role. We observed a large amplitude misfit which, for surface waves, can not be explained by scattering or focusing/defocussing effects alone. For surface waves, the scattering effects are relatively independent of period down to 40 s at least, and a large signal remains to be explained by either source effects or attenuation. We observed a clear shift in surface wave amplitude histograms particularly at short periods which is likely due to the 1-D Q model used to compute the synthetic seismograms in the crust and upper-mantle. For body waves, the largest part of the amplitude anomaly can be explained by scattering effects.

Compared to real seismograms, much signal remains unexplained in phase and amplitude. Progress in explaining the phase can only be made if we treat the crust and the mantle (and source location for body waves) simultaneously. Attenuation is notoriously difficult as demonstrated by the lack of agreement between various studies, but is essential to explain the amplitudes of surface waves. Full waveform inversion is probably the most elegant way forward, but needs to address the full elastic, anelastic and source problem.

ACKNOWLEDGMENTS

We gratefully acknowledge the availability of broad-band seismograms from the IRIS/USGS (IU), the USAF/USGS (GT) and the New China Digital Seismograph Network (IC) from USGS/Albuquerque Seismological Laboratory; the IRIS/IDA Network (II) from University of California, Scripps Institute of Oceanography; the Canadian National Seismograph Network (CN) from Geological Survey of Canada; the GEOSCOPE Network (G) from Institut de Physique du Globe de Paris; the GEOFON Network (GE) from GEOFON Program and the Pacific21 Network (PS) from University of Tokyo through the IRIS Data Management Center. We are grateful to the editor Gabi Laske and the reviewers Göran Ekström and Jeroen Ritsema for their constructive comments which significantly improved our manuscript. Guust Nolet's comments and suggestions about body wave amplitudes were very helpful. This project was funded by the European Commission's Human Resources and Mobility Program Marie Curie Research and Training Network SPICE Contract No. MRTNCT-2003-504267. Synthetic seismograms were calculated on a 128-processor cluster financed by the Dutch National Science Foundation under the grant number NWO:VICI865.03.007.

REFERENCES

Bassin, C., Laske, G. & Masters, G., 2000. The current limits of resolution for surface wave tomography in North America, *EOS, Trans. Am. geophys. Un.,* **81,** F897.

Becker, T.W. & Boschi, L., 2002. A comparison of tomographic and geodynamic mantle models, *Geochem., Geophys., Geosyst.,* **3,** doi:2001GC000168.

Bhattacharyya, J., Masters, G. & Shearer, P., 1996. Global lateral variations of shear wave attenuation in the upper mantle, *J. geophys. Res.,* **101,** 22 273–22 289.

Boschi, L. & Dziewonski, A., 1999. High and low-resolution images of the Earth's mantle: implications of different approaches to tomographic modeling, *J. geophys. Res.,* **104,** 25 567–25 594.

Bozdağ, E. & Trampert, J., 2008. On crustal corrections in surface wave tomography, *Geophys. J. Int.,* **172,** 1066–1082.

Capdeville, Y. & Marigo, J.-J., 2008. Shallow layer correction for spectral element like methods, *Geophys. J. Int.,* **172,** 1135–1150, doi:10.1111/j.1365-246X.2007.03703.x.

Cara, M., 1973. Filtering of dispersed wavetrains, *Geophys. J. R. astr. Soc.,* **33,** 65–80.

Dalton, C.A. & Ekström, G., 2006. Global models of surface wave attenuation, *J. geophys. Res.,* **111,** B05317, doi:10.1029/2005JB003997.

Dalton, C.A., Ekström, G. & Dziewonski, A.M., 2008. The global attenuation structure of the upper mantle, *J. geophys. Res.,* **113,** B09303, doi:1029/2007/B005429.

Durek, J. & Ekström, G., 1996. A radial model of anelasticity consistent with long-period surface-wave attenuation, *Bull. seism. Soc. Am.,* **86,** 144–158.

Dziewonski, A.M. & Anderson, D.L., 1981. Preliminary reference Earth model, *Phys. Earth planet. Inter.,* **25,** 297–356.

Ekström, G., Tromp, J. & Larson, E., 1997. Measurements and global models of surface wave propagation, *J. geophys. Res.,* **102,** 8137–8157.

Ferreira, A. & Woodhouse, J., 2006. Long-period seismic source inversions using global tomographic models, *Geophys. J. Int.,* **166,** 1178–1192.

Ferreira, A. & Woodhouse, J., 2007. Source, path, and receiver effects on seismic surface waves, *Geophys. J. Int.,* **168,** 109–132.

Fichtner, A., Kennett, B.L.N., Igel, H. & Bunge, H.-P., 2008. Theoretical background for continental and global scale full-waveform inversion in the time-frequency domain, *Geophys. J. Int.,* **175,** 665–685.

Gung, Y. & Romanowicz, B., 2004. Q tomography of the upper mantle using three-component long-period waveforms, *Geophys. J. Int.,* **157,** 813–830.

Kennett, B. & Engdahl, E.R., 1991. Traveltimes for global earthquake location and phase identification, *Geophys. J. Int.,* **105,** 429–465.

Komatitsch, D. & Tromp, J., 2002a. Spectral-element simulations of global seismic wave propagation—I. Validation, *Geophys. J. Int.,* **149,** 390–412.

Komatitsch, D. & Tromp, J., 2002b. Spectral-element simulations of global seismic wave propagation—II. Three-dimensional models, oceans, rotation and self-gravitation, *Geophys. J. Int.,* **150,** 303–318.

Komatitsch, D., Ritsema, J. & Tromp, J., 2002. The spectral-element method, Beowulf computing, and global seismology, *Science,* **298,** 1737–1742.

Komatitsch, D., Tsuboi, S. & Tromp, J., 2005. The Spectral-Element Method in Seismology in *Seismic Earth: Array Analysis of Broadband Seismograms* AGU Geophysical Monograph Ser., 157, pp. 205–228, eds Levander, A. and Nolet, G., Washington DC.

Montagner, J. & Jobert, N., 1988. Vectorial tomography—II. Application to the Indian Ocean, *Geophys. J. Int.,* **94,** 309–344.

Montelli, R., Nolet, G., Dahlen, F., Masters, G., Engdahl, E. & Hung, S., 2004. Finite-frequency tomography reveals a variety of plumes in the mantle, *Science,* **303,** 338–343.

Mooney, W., Laske, G. & Masters, T., 1998. Crust5.1: a global crustal model at $5^\circ \times 5^\circ$, *J. geophys. Res.,* **103,** 727–747.

Qin, Y., Capdeville, Y., Montagner, J.-P., Boschi, L. & Becker, T.W., 2009. Reliability of mantle tomography models assessed by spectral element simulation, *Geophys. J. Int.*, **177,** 125–144, doi:10.1111/j.1365-246X.2008.04032.x.

Reid, F., Woodhouse, J. & van Heijst, H., 2001. Upper mantle attenuation and velocity structure from measurements of differential s phases, *Geophys. J. Int.,* **145,** 615–630.

Resovsky, J.S., Trampert, J. & der Hilst, R.D.V., 2005. Error bars for the global seismic Q profile, *Earth planet. Sci. Lett,* **230,** 413–423.

Ritsema, J., van Heijst, H. & Woodhouse, J., 1999. Complex shear wave velocity structure imaged beneath Africa and Iceland, *Science,* **286,** 1925–1928.

Ritsema, J., Rivera, L., Komatitsch, D., Tromp, J. & van Heijst, H., 2002. The effects of crust and mantle heterogeneity on PP/P and SS/S amplitude ratios, *Geophys. Res. Lett.,* **29,** doi:10.1029/2001GL013831.

Ritsema, J., van Heijst, H.J., Woodhouse, J. & Deuss, A., 2009. Long-period body-wave traveltimes through the crust: implication for crustal corrections and seismic tomography, *Geophys. J. Int.,* **179**(2), 1255–1261.

Ritzwoller, M. & Lavely, E.M., 1995. Three-dimensional seismic models of the earth's mantle, *Rev. Geophys.,* **33,** 1–66.

Romanowicz, B., 1995. A global tomographic model of shear attenuation in the upper mantle, *J. geophys. Res.,* **100,** 12 375–12 394.

Romanowicz, B., 2003. Global mantle tomography: progress status in the past 10 years, *Annu. Rev. Earth planet. Sci.,* **31,** 303–328.

Selby, N.D. & Woodhouse, J.H., 2000. Controls on rayleigh wave amplitudes: attenuation and focusing, *Geophys. Res. Lett.,* **142,** 933–940.

Sigloch, K., McQuarrie, N. & Nolet, G., 2008. Two-stage subduction history under north america inferred from multiple-frequency tomography, *Nat. Geosci.*, **1,** 458, doi:10.1038/ngeo231.

Spetzler, J., Trampert, J. & Snieder, R., 2002. The effect of scattering in surface wave tomography, *Geophys. J. Int.,* **149,** 755–767.

Tape, C., Liu, Q. & Tromp, J., 2007. Finite-frequency tomography using adjoint methods - Methodology and examples using membrane surface waves, *Geophys. J. Int.,* **168,** 1105–1129.

Tibuleac, I.M., Nolet, G., Michaelson, C. & Koulakov, I., 2003. P wave amplitudes in a 3-D earth, *Geophys. J. Int.,* **155,** 1–10.

Trampert, J. & Spetzler, J., 2006. Surface wave tomography: finite-frequency effects lost in the null space, *Geophys. J. Int.,* **164,** 394–400.

Trampert, J. & van der Hilst, R.D., 2005. Towards a quantitative interpretation of global seismic tomography, *Geophys. Monogr.,* **160,** 47–62.

Trampert, J. & Woodhouse, J., 1995. Global phase velocity maps of Love and Rayleigh waves between 40 and 150 seconds, *Geophys. J. Int.,* **122,** 675–690.

Tsuboi, S., Komatitsch, D., Ji, C. & Tromp, J., 2003. Broadband modeling of the 2002 Denali fault earthquake on the Earth Simulator, *Phys. Earth planet. Inter.,* **139,** 305–312.

Tsuboi, S., Komatitsch, D., Ji, C. & Tromp, J., 2004. Modeling of global seismic wave propagation on the Earth Simulator, *J. Earth Simulator,* **1,** 57–66.

van Heijst, H.J. & Woodhouse, J., 1999. Global high-resolution phase velocity distributions of overtone and fundamental-mode surface waves determined by mode branch stripping, *Geophys. J. Int.,* **137,** 601–620.

Visser, K., Trampert, J. & Kennett, B., 2008. Global anisotropic phase velocity maps for higher mode Love and Rayleigh waves, *Geophys. J. Int.,* **172,** 1016–1032.

Wang, Z. & Dahlen, F., 1995. Validity of surface-wave ray theory on a laterally heterogeneous earth, *Geophys. J. Int.,* **123,** 757–773.

Warren, L.M. & Shearer, P.M., 2002. Mapping lateral variations in upper mantle attenuation by stacking p and pp spectra, *J. geophys. Res.,* **107**(B12), 2342, doi:10.1029/2001JB001195.

Woodhouse, J. & Wong, Y., 1986. Amplitude, phase and path anomalies of mantle waves, *Geophys. J. R. astr. Soc.,* **87,** 753–773.

Zhou, Y., 2009. Surface-wave sensitivity to 3-D anelasticity, *Geophys. J. Int.,* **178**(3), 1403–1410.

Zhou, Y., Dahlen, F., Nolet, G. & Laske, G., 2005. Finite-frequency effects in global surface-wave tomography, *Geophys. J. Int.,* **163,** 1087–1111.